Multifunctional Liquid Crystal Nanoparticles for Intracellular Fluorescent Imaging and Drug Delivery

Christopher M. Spillmann,[†] Jawad Naciri,[†] W. Russ Algar,[†,‡,§] Igor L. Medintz,[†] and James B. Delehanty[†,*]

[†]Center for Bio/Molecular Science and Engineering, Naval Research Laboratory, 4555 Overlook Avenue Southwest, Washington, D.C., 20375, United States and [‡]College of Science, George Mason University, 4400 University Drive, Fairfax, Virginia 22030, United States [§]Present address: Department of Chemistry, University of British Columbia, 2036 Main Mall, Vancouver, British Columbia V6T 1Z1, Canada.

ABSTRACT A continuing goal of nanoparticle (NP)-mediated drug delivery (NMDD) is the simultaneous improvement of drug efficacy coupled with tracking of the intracellular fate of the nanoparticle delivery vehicle and its drug cargo. Here, we present a robust multifunctional liquid crystal NP (LCNP)-based delivery system that affords facile intracellular fate tracking coupled with the efficient delivery and modulation of the anticancer therapeutic doxorubicin (Dox), employed here as a model drug cargo. The LCNPs consist of (1) a liquid crystal cross-linking agent, (2) a homologue of the organic chromophore perylene, and (3) a polymerizable surfactant containing a carboxylate headgroup. The NP core provides an environment to both incorporate fluorescent dye for spectrally tuned particle tracking and encapsulation of amphiphilic and/or hydrophobic agents for intracellular delivery. The carboxylate head groups enable conjugation to biologicals to facilitate the cellular uptake of the particles. Upon functionalization of the NPs with transferrin, we show the ability to differentially label the recycling endocytic pathway in HEK 293T/17 cells in a time-resolved manner with minimal cytotoxicity and with superior dye photostability compared to traditional organic fluorophores. Further, when passively loaded with Dox, the NPs mediate the rapid uptake and subsequent sustained release of Dox from within endocytic vesicles. We demonstrate the ability of the LCNPs to simultaneously serve as both an efficient delivery vehicle for Dox as well as a modulator of the drug's cytotoxicity. Specifically, the delivery of Dox as a LCNP conjugate results in a ~40-fold improvement in its IC_{50} compared to free Dox in solution. Cumulatively, our results demonstrate the utility of the LCNPs as an effective nanomaterial for simultaneous cellular imaging, tracking, and delivery of drug cargos.

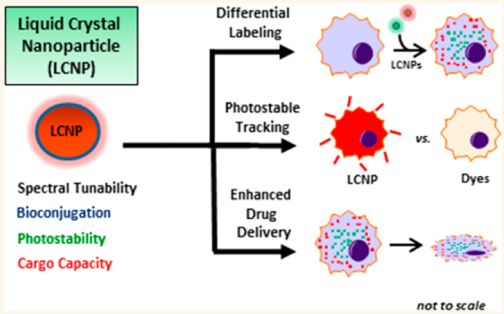

KEYWORDS: nanoparticle · drug delivery · doxorubicin · bioconjugation · liquid crystal · fluorescent microscopy

The burgeoning field of nanoparticle (NP)-mediated drug delivery (NMDD) offers much to overcome many of the issues associated with the systemic delivery of conventional therapeutics, particularly those that are insoluble or highly toxic.[1,2] As this nascent field is still predominantly in the research phase, a key requirement continues to be the development of "prototypical" nanoparticle materials that can be extensively utilized to design, characterize, improve and provide all the necessary knowledge for understanding how NPs and their cargos interact with targeted cells.[3,4] Ideally, such prototypical NPs would provide several key features including (1) facile, large-scale synthesis of relatively small NPs (diameter ≤ 100 nm) characterized by monodisperse populations, (2) amenability to bioconjugation for delivery to and uptake by targeted cells, (3) a core environment favoring the hosting of amphiphilic and/or hydrophobic agents, (4) low cytotoxicity and (5) the ability to monitor and track the particles with both spatial and temporal resolution. One effective means to achieve the latter feature is *via* fluorescence, yet incorporating this functionality has its own set of ideal requirements. These include high quantum yield, long-term photo- and chemical stability and a tunable spectral output to allow for multiplexing, *i.e.*, simultaneous monitoring of multiple colors.

Although there are several available and well-characterized NP materials that do provide some combination of the above properties, each of these materials are also hindered by several liabilities. For example, luminescent semiconductor quantum dots

* Address correspondence to james.delehanty@nrl.navy.mil.

Received for review April 2, 2014 and accepted June 30, 2014.

Published online June 30, 2014
10.1021/nn501816z

are technically challenging to synthesize, are not that easily bioconjugated and are still plagued by concerns surrounding their long-term toxicity *in vivo*.[5] Although quite promising, fluorescent gold nanoclusters are not fully understood and generally manifest rather modest quantum yields.[6,7] Commercial dye-impregnated microspheres tend to be quite large in size, thus rendering cellular uptake a formidable task,[8,9] and they do not offer the possibility of sustained release of drug cargos.

We have previously reported on the synthesis and physical characterization of liquid crystal-based NPs that manifest many of the desirable photophysical properties described above.[10] These fluorescent NPs, referred to herein as liquid crystal nanoparticles (LCNPs), provide multifunctionality by marrying three molecular components into a single NP composite: (1) a nematic diacrylate liquid crystalline cross-linker, (2) a derivative of the chromophore perylene and (3) a polymerizable monoacrylate amphiphile with a carboxylate headgroup that caps the nanoparticle. The LCNPs are synthesized using an established miniemulsion technique to thermally polymerize the components and create stable NP materials as an aqueous colloidal suspension.[10,11] By varying the mole ratio of perylene to diacrylate liquid crystal, the aggregation number of the perylene chomophore within the particle is discretely controlled, thereby allowing the peak fluorescent emission to be tuned over a wide range of the visible spectrum (~540−620 nm).[10] The incorporation of perylene into the LCNPs provides high quantum yield (increasing from ~0.6 to a remarkable 1.0 as the peak emission is blue-shifted) and imparts photo- and chemical stability, an important characteristic for their usefulness in fluorescence-based biological applications. Additionally, the headgroup of the surfactant allows conjugation of the LCNPs to a range of biomolecules *via* standard EDC chemistry. As a proof of principle, we have previously demonstrated the effectiveness of the LCNPs as a fluorescent tracer in a sandwich immunoassay for the detection of the protein toxin ricin.[11]

In this report, we evaluate the utility of these designer nanomaterials for targeted cellular uptake, long-term multicolor fluorescence labeling/tracking and the delivery of the amphiphilic anticancer drug doxorubicin (Dox). Differentially emissive nanoparticles were synthesized and covalently coupled to the iron transport protein transferrin (Tf) to facilitate their endocytic uptake by human embryonic kidney (HEK 293T/17) cells. We then use a time-resolved delivery strategy to realize the multicolor labeling of distinct cross sections of the recycling endocytic pathway and show the superior photostability of the materials relative to traditional probes for tracking the endocytic pathway in these same cells. Finally, we demonstrate that when passively loaded with Dox, the LCNP-Tf conjugates effectively deliver the drug to the nucleus of HEK 293T/17 cells, resulting in the controlled modulation of the cytotoxicity of this widely used, yet highly toxic, cancer therapeutic. The delivery of Dox as a LCNP-Tf conjugate results in a ~40-fold improvement in its IC_{50} (when expressed in terms of NP concentration) compared to when Dox is delivered free in solution. Such improvements have been difficult to attain and are strongly dependent on the NP formulation used for Dox delivery.[12] Cumulatively, our work presented here demonstrates the utility of LCNPs as an efficacious new nanomaterial for simultaneous cellular labeling, tracking and drug delivery.

RESULTS

Synthesis and Characterization of LCNPs. Aqueous colloidal suspensions of LCNPs were synthesized using a two-phase miniemulsion technique as described previously.[10] They consist of a perylene derivative (PERC11), a liquid crystalline cross-linking agent (DACTP11) and a monoacrylate carboxylate headgroup (AC10COONa). The chemical structure of each component molecule is shown in Figure 1A. Heating of the emulsion induces thermal polymerization of the acrylates, thus creating a polyacrylate nanoparticle primarily composed of DACTP11 and capped with AC10COONa. A schematic of this process is shown in Figure 1B. The inclusion of perylene provides a strong fluorescence signature to

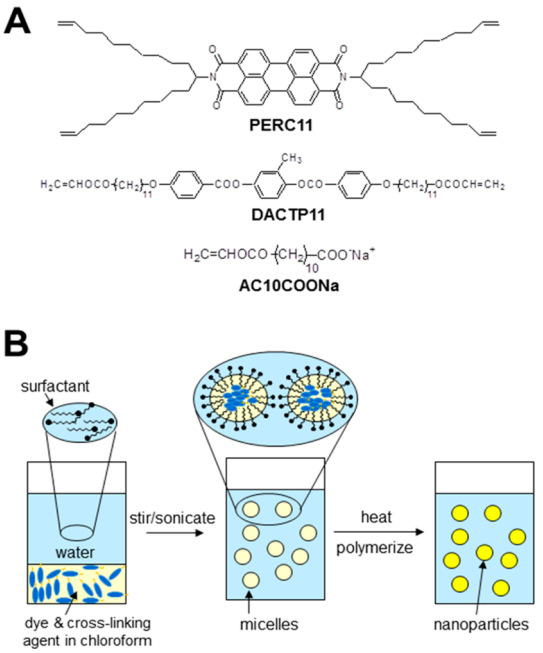

Figure 1. Liquid crystal nanocolloids (LCNPs). (A) Nanocolloids are comprised of a perylene-based dye (PERC11), an acrylate liquid crystal cross-linking agent (DACTP11) and a carboxyl-terminated polymerizable surfactant (AC10COONa). (B) Miniemulsion process used to synthesize colloidal nanoparticles in an aqueous suspension. Stirring and sonication of the two-phase water−organic system results in micelle encapsulation of the dye and cross-linker and capping of the micelles with surfactant. Subsequent thermal polymerization stabilizes the micelles into nanoparticles.

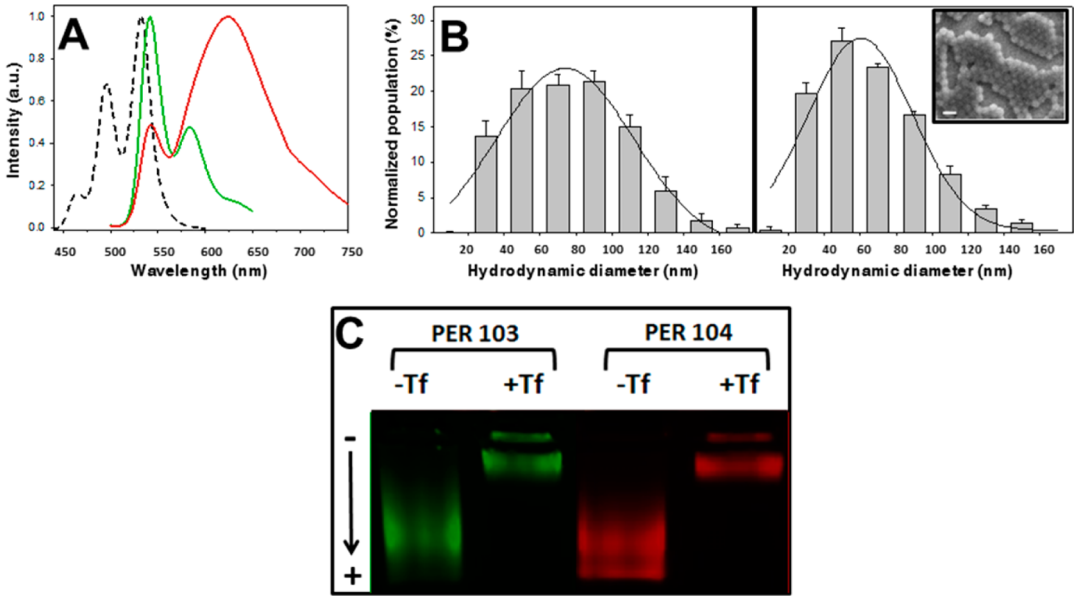

Figure 2. Characterization of LCNPs and LCNP bioconjugates. (A) LCNP spectra showing the absorption spectrum (dashed black line) and the fluorescence emission spectra of the PER103 (green) and PER104 (red) LCNPs used in this study. (B) Size distribution of LCNPs. Nanoparticle size distribution of PER103 (left) and PER104 (right) LCNPs as determined using a Nanosight Particle Tracking System. Error bars represent standard deviation of three experimental preparations. Inset: SEM image of nanoparticles (scale bar, 100 nm). (C) Conjugation of LCNPs to human transferrin (Tf). Conjugates were analyzed by 1.5% agarose gel electrophoresis. Unconjugated NPs (−Tf) migrate toward the cathode (+), while Tf-conjugated NPs (+Tf) display minimal electrophoretic mobility and remain at the anode (−).

the LCNPs. As previously reported, the mole percentage of perylene dye relative to the DACTP11 crosslinker can be varied to control the aggregation number of the dye, resulting in tuning of the peak fluorescence emission between 540 and 620 nm (under 488 nm excitation).[10] Two LCNP species were used in these studies, referred to as PER103 and PER104. In the PER103 and PER104 LCNPs, the mole percentage of PERC11 relative to DACTP11 was 0.5 and 4.1%, respectively. This resulted in well-separated peak emissions at 540 and 620 nm (Figure 2A), thus allowing for the two LCNP populations to be spectrally resolved with standard fluorescence filter sets (see Supporting Information (SI)). At the mole percentages of PERC11 incorporated into each population, the quantum yields of PER103 and PER104 were calculated to be 1.0 and 0.7, respectively. Following centrifugation of the colloidal suspension to reduce both the size and the inherent polydispersity from synthesis, the average hydrodynamic diameter of the LCNP samples were determined using Nanosight Tracking Analysis. The results showed the average particle diameter to be ∼60−70 nm (Figure 2B), which was confirmed using SEM (Figure 2B, inset).

Bioconjugation and Cellular Uptake of LCNP-Tf Conjugates. To facilitate the cellular uptake of the LCNPs for labeling and imaging, human transferrin (Tf) was conjugated to the available terminal carboxyl functional groups of the solubilizing surfactant using carbodiimide chemistry. Analysis by gel electrophoresis confirmed the successful conjugation of Tf to both the PER103 and PER104 LCNPs as the resulting bioconjugates exhibited a significantly reduced migration compared to the unconjugated control LCNPs (Figure 2C). These results confirmed the consumption of free carboxyl groups on the LCNP surface due to conjugation. Given the average LCNP surface area of 1.3×10^4 nm^2 (average NP diameter ∼65 nm), the surface area of Tf available to contact the NP surface (∼47 nm^2)[13] and an average valence of ∼15 Tf per LCNP (see Materials and Methods), this corresponds to ∼6% coverage of the NP surface by the appended Tf molecules.

The decoration of the LCNPs with Tf facilitated their specific uptake by HEK 293T/17 cells, as shown in Figure 3A. Incubation of the LCNP-Tf conjugates (50 nM) with cell monolayers for 1 h resulted in their endocytosis and a classical punctate and perinuclear morphology that is characteristic of Tf-mediated NP uptake.[14−18] Under these conditions, an uptake efficiency of ∼75% was routinely observed across multiple delivery experiments. Similar cell uptake results were obtained with Tf conjugates of PER104. The cellular uptake of the LCNPs was specific for the presence of the Tf ligand as no detectable fluorescence was observed in the LCNP channel for the Tf-free NPs, indicating minimal nonspecific binding of the as-synthesized NPs to either the plasma membrane or cell surface receptors/moieties over the incubation time regimes employed here (SI, Figure S2). Additionally, the presence of soluble transferrin during incubation of the LCNP-Tf conjugates with cell monolayers inhibited binding and subsequent uptake of the conjugates (SI, Figure S2). Further, control imaging experiments

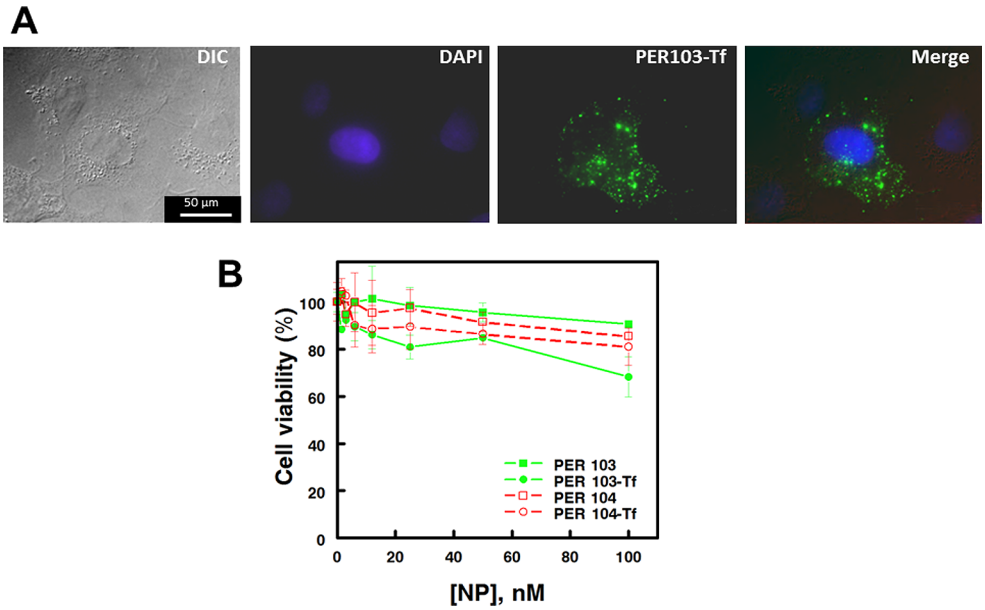

Figure 3. Cellular delivery of LCNP-transferrin conjugates. (A) Cellular uptake of LCNP-Tf conjugates. PER103 LCNPs conjugated to transferrin (PER103-Tf) were incubated at 50 nM (final LCNP concentration) with HEK 293T/17 cell monolayers for 1 h followed by fixation, staining and imaging as described in Methods. Images correspond to differential interference contrast (DIC), nuclei (DAPI), LCNP (PER103-Tf) and merge. Scale bar, 50 μm. (B) Cytotoxicity of LCNP-Tf conjugates. Shown are cellular viabilities of HEK 293T/17 cells after 1 h incubation with LCNPs or LCNP-Tf conjugates (and subsequent 72 h culture) as determined by MTS assay.

showed no detectable crosstalk between the PER103 and PER104 channels employing the image acquisition parameters used for imaging the Tf conjugates (SI, Figure S3). This latter observation is a critical requirement for performing the two-color labeling/tracking experiments detailed herein (*vide infra*). Finally, but no less important, the LCNPs and their corresponding Tf conjugates were well tolerated by HEK 293T/17 cells, showing only modest effects on cellular proliferation. Standard cytotoxicity assays (MTS) showed that cells incubated with both Tf-free LCNP species exhibited cell viabilities of ~90% at the highest concentration tested (100 nM), while at the 50 nM concentration used for delivery experiments, the PER103-Tf and PER104-Tf conjugates showed comparable effects on cellular proliferation (Figure 3B).

LCNP-Tf-Mediated Differential Labeling of the Recycling Endocytic Pathway. Having established the efficient and specific Tf-mediated cellular uptake of the LCNPs, our goal was to next use these conjugates in a combinatorial fashion to take advantage of their superior photostability for extended differential labeling and tracking of the endocytic pathway. Here, we leveraged our previous spatiotemporal labeling approach where we demonstrated the ability to differentially label early and late endosomal vesicles in a spatiotemporal manner using QDs appended with polyarginine cell penetrating peptides, proteins or commercial transfection reagents, respectively.[19,20] As shown in Figure 4A, when both LCNP-Tf conjugates (50 nM) were incubated simultaneously with HEK293T/17 cell monolayers for 30 min, a nearly identical staining morphology was observed in both the PER103-Tf and PER104-Tf channels, indicating a high degree of coloading of the NPs within the same endocytic vesicles. This coloading was evidenced by the significant amount of yellow colocalization in the merged image panel and confirmed by quantitative image analysis which showed ~89% colocalization of the green and red signals (SI, Table S2). When a staggered delivery regimen was employed, however, it was clear that distinct cross sections of endocytic vesicles could be labeled with the materials. For example, loading the cells with the green-emitting PER103-Tf materials first and then culturing the cells in growth media for ~18 h followed by delivery of the red-emitting PER104-Tf LCNPs resulted in a significant decrease in the degree of colocalization to ~49%, indicating the labeling of distinct endocytic compartments (Figure 4B, SI Table S2). The converse experiment (*i.e.*, delivery of red-emitting NPs followed by green-emitting) yielded comparable colocalization results; the degree of overlap was reduced to ~53% (Figure 4C, SI Table S2). In both delivery iterations, we observed no deleterious effects on the fluorescence emission or brightness of either LCNP species, even when the LCNPs were delivered first and then cultured intracellularly (localized within the slightly acidic endosomal compartments) for 18 h. This result demonstrated the remarkable intracellular chemical and photostability of the materials and prompted us to directly compare their intracellular photostability to commercial preparations of AlexaFluor-transferrin conjugates. These materials are among the most commonly used probes for tracking the recycling endocytic pathway.[21]

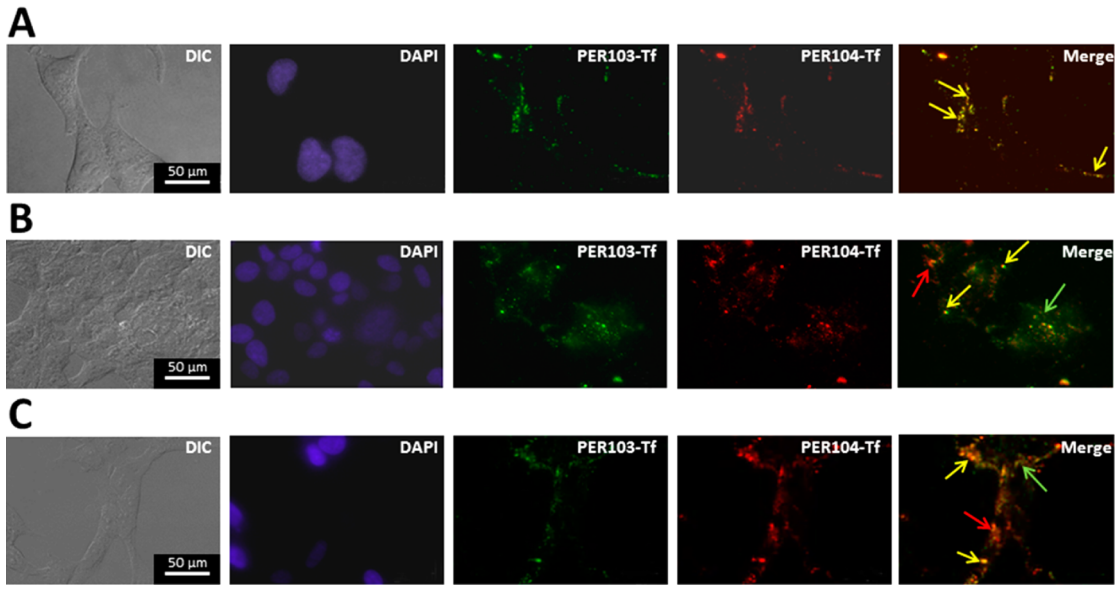

Figure 4. Differential labeling of the recycling endocytic pathway with LCNP-transferrin conjugates. Endosomal compartments of HEK 293T/17 cells were labeled with 50 nM PER103-Tf (green) and 50 nM PER104-Tf (red) conjugates. (A) Two-color simultaneous delivery and labeling of endosomes. (B,C) Two-color, staggered delivery and labeling: (B) PER103-Tf, day one/PER104-Tf, day two; (C) PER104-Tf, day one/PER103-Tf, day two. Shown are DIC, DAPI, PER103- and PER104-Tf channels and merged fluorescence images of the LCNP channels. Yellow arrows indicate regions of colocalization of the two LCNP species; green and red arrows correspond to areas of noncolocalization where the color of the arrow indicates the predominate color at that location.

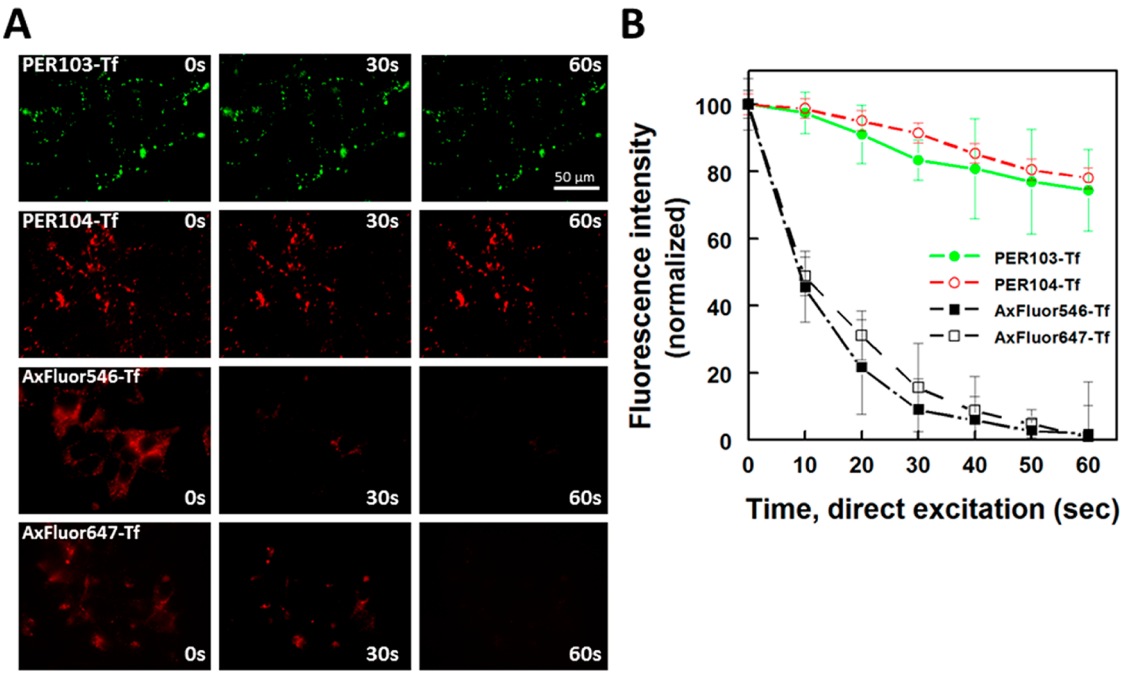

Figure 5. LCNP-transferrin conjugates display superior intracellular photostability compared to organic dye-transferrin conjugates. (A) Fluorescent micrographs of the time-resolved fluorescence intensities of intracellular PER103-Tf, PER104-Tf, AxFluor 546-Tf and AxFluor647-Tf conjugates under continuous excitation with a Xe arc lamp. (B) Quantification of the time-resolved fluorescence intensities for the images in (A). Data shown are the average ± SD of at least 10 regions of interest in each image. AxFluor = AlexaFluor. Scale bar, 50 μm.

As shown in Figure 5A, under conditions of constant illumination by the Xe arc lamp both LCNP-Tf materials displayed superior extended photostability compared to AlexaFluor-546 and 647 conjugates of Tf. Quantification showed that the LCNPs retained ~80% of their fluorescence intensity over the 60 s illumination time frame, while the fluorescence emission of both organic dye Tf conjugates was completely bleached (Figure 5B).

LCNP-Tf-Mediated Dox Delivery and Cytotoxicity. Given their excellent cellular uptake, labeling and photostability properties, we sought to take advantage of

the hydrophobic nature of the LCNP core to act as a host for doxorubicin (Dox), an amphiphilic chemotherapeutic, for simultaneous multicolor NP-mediated drug delivery and tracking. Our aim was to use the π-stacked environment of the LCNP to drive the partitioning of the Dox into the NP core. We employed the PER104-Tf LCNPs as the NP delivery vehicle as its emission spectrum was sufficiently red-shifted to be distinct from that of Dox, eliminating channel crosstalk with appropriate filter sets (SI Figures S1, S3). Given the ample surface area available on the LCNP surface after conjugation to Tf (est. >90%) and the sufficiently hydrophobic nature of Dox (log $P = 2.82$),[22] we expected efficient sequestration of the Dox within the LCNP core. After incubating the LCNPs in D-PBS with a molar excess of Dox, the removal of unincorporated Dox by size-exclusion chromatography resulted in PER104-Tf NPs with $\sim 50 \pm 9$ Dox molecules associated per NP as determined by differential absorbance spectroscopy (SI, Figure S4).

Cellular delivery experiments next confirmed the successful cellular uptake of NPs carrying the Dox cargo and its subsequent intracellular release. The fluorescence micrographs in Figure 6A show the resulting time-resolved signals of the LCNP-Tf conjugates and the Dox cargo at various time points after initial incubation of the complexes with cell monolayers. Here, 50 nM PER104-Tf LCNPs carrying a Dox cargo ($\sim$2.5 μM total Dox load) were incubated with HEK 293T/17 cells for 1 h. After removing the NPs, the cells were then cultured in growth medium for various time points to allow for the passive efflux of Dox from the LCNP core. As expected, 2 h after this initial incubation period the PER104-Tf NPs were localized within endosomes, indicating no inhibitory effect on cellular NP uptake by the Dox cargo. Notably, the Dox signal was completely colocalized with the LCNP signal, demonstrating the sequestration of the Dox within the same endosomal compartments. In contrast, control experiments showed that after a 2 h incubation with free Dox (1 μM), a measurable fluorescence signal of DNA-bound Dox was already apparent in the nucleus, and this signal continued to increase in a dose- and time-dependent manner (SI, Figure S5A). Such kinetics for free Dox uptake are consistent with previous reports.[23] Dox internalization was also coupled with a concomitant decrease in nuclear size due to chromatin condensation (SI, Figure S5B).[24−26] A similar endosomal colocalization of the LCNPs and Dox was observed at 4 h. Additionally, DIC imaging showed no aberrations in cellular appearance; cells displayed their typical flattened, attached morphology. At 12 h, however, a distinct separation of the NP and Dox signals was observed, with the LCNP signal remaining exclusively punctate/endosomal while the Dox fluorescence was a mixture of punctate and diffuse, consistent with the retention of a portion of the Dox in endosomes while a percentage escaped and entered the nucleus. Dox presumably enters the nucleus *via* its diffusion through the nuclear pore complexes of the nuclear membrane.[27] We also noted an increase in the number of rounded/clumped, loosely adherent and fully detached cells at this point, clear evidence of Dox-induced cytotoxicity.[28,29] At 48 h, the LCNPs remained fully endosomal while the Dox signal was increasingly nuclear in appearance, although a portion of the Dox signal still remained within endosomes. Notably, a significant loss of cells due to total cellular detachment occurred making it difficult to locate fields containing more than two to three cells during imaging, clear evidence once again of Dox-induced cell death at this time point.

To determine the kinetics of nuclear accumulation of LCNP-Tf-delivered Dox, we compared the time-resolved fluorescence intensities of the nonendosomal/nuclear Dox when delivered *via* the NPs to those corresponding to the nuclear accumulation of free Dox. Similar fluorescence-based approaches have been described for intracellular Dox quantification.[30] The data in Figure 6B clearly show the disparity in kinetics of Dox nuclear accumulation between free Dox *versus* when Dox was delivered as a PER104-Tf NP complex. Dox taken up from bulk solution displayed linear nuclear accumulation kinetics while the LCNP-Tf-delivered Dox followed a sigmoidal trajectory. While completely endosomal through 4 h, at the 12 h time point the intensity of the nuclear Dox signal delivered from the NPs approached that of $\sim$1 μM free Dox and did not increase beyond that level through 48 h. Punctate Dox signal remained evident even at the 48 h time point indicating that not all of the Dox had been released from within endosomes. These data support the sustained, passive efflux of the Dox from within the LCNP core and strongly suggest that most if not all of the NP-associated Dox was originally contained within the LCNP core. Were the majority of the Dox merely nonspecifically associated with the NP surface, a more linear kinetic profile of its nuclear accumulation approximating that of free Dox would have been expected. These data also demonstrate that not all of the LCNP-loaded Dox was released from within endosomes, a characteristic that has been observed in other NP-based Dox delivery systems.[12]

Finally, we compared the effects of free Dox delivery *versus* LCNP-Tf delivered Dox on cellular proliferation by performing MTS cytotoxicity assays on various permutations of the PER104 LCNP and Dox materials. As shown in Figure 6C, the PER104 and Tf conjugates of PER104 elicited minimal effect on cellular viability, confirming our previous results (see Figure 3). The delivery of free Dox yielded an IC_{50} of 151 ± 42 nM, in good agreement with published values attained across a variety of cell lines.[12,31,32] The delivery of Dox as a LCNP complex, however, clearly demonstrated the ability of the NP to not only mediate Dox-induced cytotoxicity but to also modulate the IC_{50} of

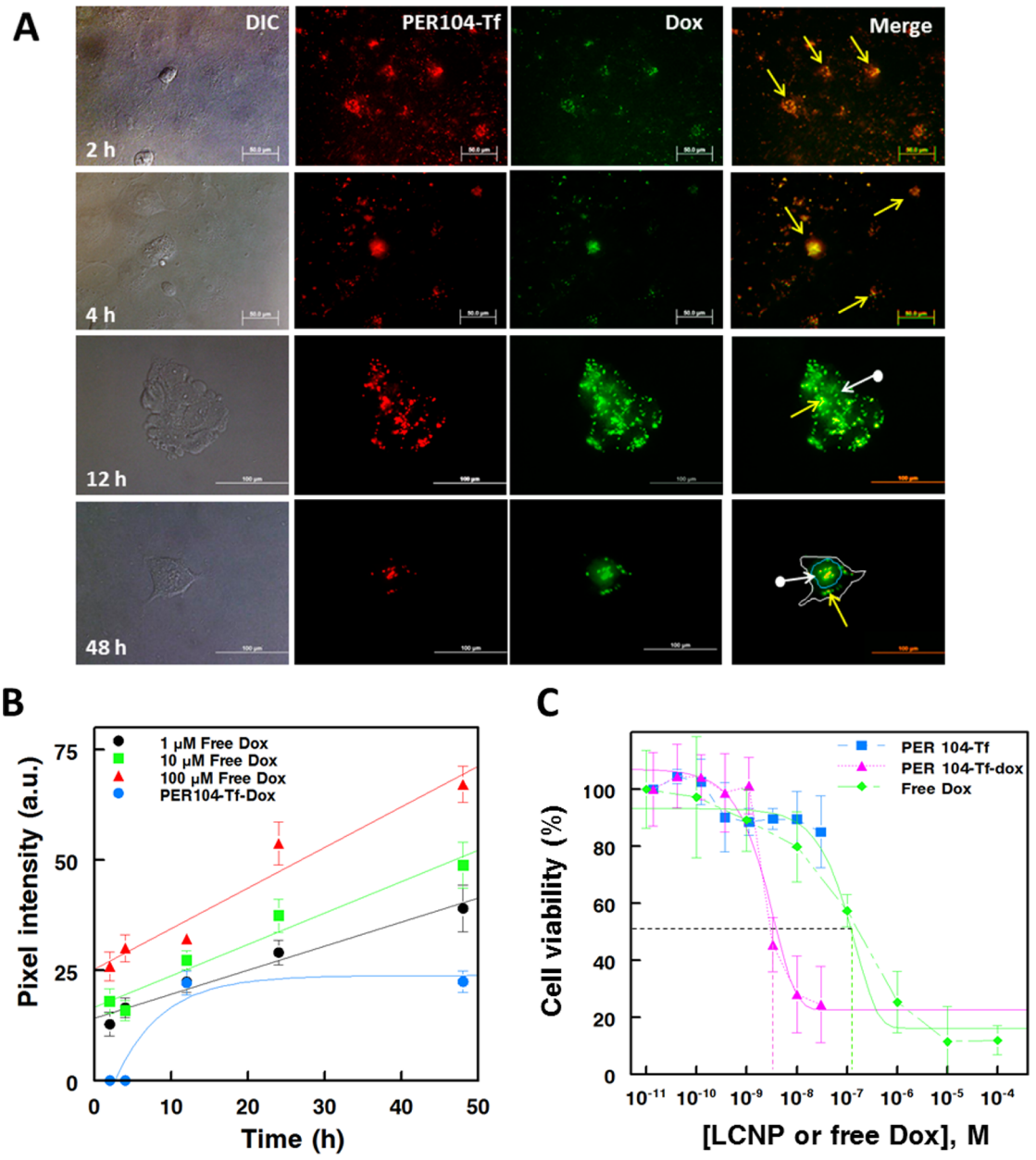

Figure 6. Time-resolved assessment of cellular uptake of Dox-loaded PER104-Tf LCNPs and associated cytotoxicity. (A) Time-resolved fluorescence tracking of intracellular PER104-Tf and Dox. Shown are DIC, fluorescence images of the PER104-Tf and Dox channels and merged images of the fluorescence channels. At 2 and 4 h after initial incubation with the materials, the PER104-Tf and Dox signals are colocalized within endosomes and punctate (yellow merged color indicated by yellow arrows). At 12 h a separation of the PER104-Tf signal from the Dox signal was observed. At 48 h the free Dox signal adopted a clearly nuclear morphology, while a portion of the Dox remained sequestered within endosomes colocalized with PER104-Tf. Yellow arrows denote colocalized LCNP and Dox signal, while white arrows (circle tail) indicate diffuse Dox signal that is separated from the punctate LCNP signal. For clarity, a representative cell is shown with its cell periphery outlined in white and the nucleus outlined in blue. Scale bars: 2 h and 4 h, 50 μm; 12 h and 48 h, 100 μm. (B) Quantitation of intracellular Dox fluorescence. The time-resolved average pixel intensities of the nonendosomal/nuclear Dox signal delivered *via* PER104-Tf LCNP conjugates were plotted along with those corresponding to Dox delivered free in solution (SI, Figure S5A) to estimate the nuclear Dox concentration attained *via* delivery as a PER104-Tf LCNP complex. Analysis shows the average pixel intensities $\pm$ SD of multiple ROIs from a minimum of 30 cells. The data are representative of experiments performed in duplicate. (C) Quantification of PER104-Tf-mediated Dox cytotoxicity. PER104-Tf, PER104-Tf-Dox or free Dox were incubated on HEK 293T/17 cell monolayers for 1 h and then the media was removed. PER104-Tf-Dox contained ~50 Dox molecules per LCNP. Cells were washed and cultured in growth medium for 72 h prior to MTS assay. Curvefits were performed by a fit of the data to a sigmoidal function to determine the IC_{50}. Dashed lines indicate the IC_{50} values for LCNP-Tf-Dox (magenta) and free Dox (green).

Dox in a controlled manner. Delivery of Dox as a LCNP-Tf conjugate yielded an IC_{50} of 3.5 $\pm$ 1.2 nM (expressed in terms of LCNP concentration) which corresponds to ~180 nM Dox taking into account the Dox loading per NP. Of particular note, this IC_{50} value corresponds to a PER104-Tf concentration at which HEK 293T/17

cellular viability was ~90% for the unloaded NPs, clearly demonstrating the ability of the LCNP materials to serve as an effective Dox delivery system at a concentration at which the NPs are largely innocuous to cellular health and viability.

DISCUSSION AND CONCLUSIONS

A chief aim of nanotechnology continues to be the development of multipurpose NP materials capable of simultaneously performing a range of disparate functionalities within biological settings (*e.g.*, cells, tissues, whole organisms). Among the list of desired capabilities are cellular targeting, labeling/imaging, structure tracking and drug/cargo delivery coupled with minimal off-target toxicity. To achieve this requires the marrying of colloidally stable, brightly fluorescent (or otherwise reportable) and photostable NP materials with biologicals (*e.g.*, peptides, proteins) for cellular targeting while simultaneously incorporating a cargo-carrying capacity. To date, approaches to realize such materials have resulted in a range of NP formulations, each having their own inherent benefits and liabilities. Fluorescent dye-doped microspheres,[33,34] supported lipid bilayers,[35] silica NPs[36] and liposomes[37,38] comprise rather large NPs (diameter 100 nm—several microns) which can impact cellular uptake and subcellular targeting.[8,9] Further, details of their drug release kinetics are only poorly understood. And while smaller NP constructs such as QDs[39] and fluorescent gold nanoclusters[40] have been shown to carry therapeutic cargos, the small surface area of these "hard" NPs limits their overall drug loading capability. Clearly, these limitations suggest a need for new NP formulations to begin to overcome these issues.

In an attempt to address these limitations, we sought to determine the potential utility of a new class of colloidal NP, liquid crystal nanocolloids (LCNPs), as a new multifunctional nanomaterial. Developed in our laboratory, these fluorescent NP constructs employ a liquid crystal cross-linker within a nanocolloid structure to control the aggregation number of a highly fluorescent perylene dye. In recent years, liquid crystal moieties have found increasing uses in biological imaging applications that extend beyond their traditional use in imaging displays and microscopy filters.[41] These include the visualization of surface-immobilized oligonucleotides[42] and the analysis of integrin receptor—substrate interactions on the cell surface.[43,44] Yet, the interfacing of liquid crystal-containing materials with living cells for *intracellular* imaging and tracking remains largely unexplored. In the nanocolloid system described here, the liquid crystal component serves multiple roles. First, it stabilizes the fluorophore in either a monomeric or in a range of stacked orientations. Increasing the aggregation state of the perylene dye results in a red shift of the NP emission; thus, the liquid crystal serves to spectrally tune the NP emission. We have previously taken advantage of the brightness and photostability of these materials to generate fluorescent labels for use in sensitive sandwich immunoassays.[11] Second, the liquid crystal core of the LCNP provides a suitably hydrophobic environment for the partitioning of amphiphilic drug cargos. This hydrophobic environment coupled with the ~60 nm diameter of the LCNPs seeks to strike a balance between extremely large NP size (hundreds of nm to μm regime) that can negatively impact cellular uptake[8,9] and cargo carrying capacity. Finally, the liquid crystal core serves to structure and present water miscible surface ligands to the NP surface where they are available for attachment to biological moieties for cellular uptake.

In the present study, we selected Tf as the model biological ligand for conjugation to the LCNPs for several reasons. First, the role of Tf in the cyclic extracellular binding of and intracellular transport of iron is well characterized[45,46] and the endocytic pathway remains the chief route of cellular uptake for most NP materials and their surface-appended or interior-loaded cargos. Methods for labeling and tracking of the endocytosis machinery have typically relied on fluorophore conjugates[21,47] or fluorescent protein fusions[48] of Tf (or other protein markers of the endocytic pathway (*e.g.*, Rab5[49] or early endosomal antigen 1[50]). Such approaches are potentially limited by the poor quantum yields or photobleaching of the fluorophore label and while studies employing Tf conjugates of more photostable materials (*e.g.*, QDs[51] or long-lifetime lanthanide chelates[52]) have been reported, the latter materials lack the cargo carrying capacity of the LCNPs used here. Conjugation to Tf afforded the specific uptake of the LCNP conjugates in a manner that elicited minimal cytotoxicity at the 50—100 nM concentrations required for robust cellular labeling. Importantly, the liquid crystal-based spectral tuning of different LCNP populations coupled with Tf conjugation and staggered delivery regimes allowed for the differential time-resolved labeling of distinct cross sections of recycling endosomes. In contrast to our previous work where different ligand moieties (*e.g.*, cell penetrating peptides and lipid-based transfection reagents) were used to discern different populations of endocytic vesicles with different QD populations,[19] our approach herein utilized a single ligand system, letting our choice of delivery time dictate vesicle labeling and eliminating the need to develop bioconjugation strategies for multiple different biologicals. Thus, it represents a simplified strategy for achieving time-resolved, two-color cellular compartmental labeling. That the LCNPs exhibit superior photostability compared to traditional labeling fluorophores during imaging is equally important, and this may be relevant to continued interest in using single particle tracking for visualizing intracellular vesicle transport and trafficking.[53]

Perhaps the most exciting aspect of the LCNPs for cellular imaging is their drug-carrying capacity as demonstrated here. We selected Dox as our model

drug cargo for this study not only because of its ability to be visualized *via* its fluorescence but also because there is continued interest in developing new cellular targeting/delivery regimes for this first-line chemotherapeutic. Dox, while potent in the treatment of many cancers (including cancers of the lung, ovary and breast), manifests severe cardiotoxicity and other off-target effects that limits its prolonged therapeutic use.[54] Our approach was to take advantage of the amphiphilic nature of the Dox and the hydrophobic interior of the LCNP to drive partitioning of Dox into the core of the as-synthesized LCNPs. In contrast to other strategies that incorporate drug cargos during NP synthesis (*e.g.*, encapsulation[55,56]), which can result in loss of drug efficacy, our strategy avails passive partitioning of the drug cargo in to the NP post-NP synthesis followed by facile separation. This strategy resulted in LCNPs with ~50 Dox molecules loaded per NP and delivery of these complexes clearly showed a time-resolved cellular uptake and intracellular/nuclear distribution that was distinct from the kinetics of free Dox uptake and nuclear accumulation; the presence of Dox in the nucleus was observed as early as 12 h after initial delivery. This provided strong evidence of successful loading of Dox into the LCNP core. Importantly, the release kinetics of Dox from within the LCNP-Tf conjugates represents an improvement from other recently reported NP-based Dox delivery systems. For example, using rod-shaped campothecin-containing NPs in which Dox was encapsulated into the NP's protein corona, Barua *et al.* observed nuclear Dox at 20 h after initial incubation.[30] It was also evident that not all of the LCNP-loaded Dox was liberated intracellularly, as a portion of the Dox remained sequestered within endosomes 48 h after the initial delivery of the LCNP-Tf-Dox conjugates. Still, cellular proliferation assays showed a remarkable ~40-fold improvement in Dox-mediated cell killing when the drug was delivered as a LCNP-Tf conjugate. Additionally, this was achieved at a NP concentration at which the drug-free LCNP-Tf conjugates were largely innocuous to cells (cellular viability ~90%). These results are exciting given the fact that not all NP formulations of Dox have been able to achieve this.[12] Further, our results open the possibility for the incorporation of actuatable moieties into the LCNP core to elicit the on-demand release of Dox or other loaded cargos in response to specific cellular stimuli.

In this work, we have introduced a new functional nanomaterial with demonstrated utility for the simultaneous imaging, tracking and drug delivery in mammalian cells. The advantages of this NP system include: their ease of synthesis and bioconjugation, small size, physical and photostability, tunability of their fluorescent emission and the ability to partition amphiphilic cargos to the core of the as-synthesized NP for efficient drug delivery at nontoxic NP concentrations. Cumulatively, these qualities make the LCNPs an ideal NP system for furthering our understanding of how to exert fine control over materials at the nanoscale within the context of living cells. Detailed knowledge of how to more actively exert control over the release kinetics of LCNP-embedded drugs (and other theranostic cargos) will further our ability to realize tailored smart materials for a range of NP-drug delivery applications.

MATERIALS AND METHODS

Materials. The nuclear stain DAPI (4′,6-diamidino-2-phenylindole), paraformaldehyde, HEPES (4-(2-hydroxyethyl)-1-piperazineethanesulfonic acid) buffer, doxorubicin hydrochloride and human transferrin were all purchased from Sigma (St. Louis, MO) and used as received. Dulbecco's phosphate buffered saline (D-PBS), DMEM containing 25 mM HEPES (DMEM-HEPES) and AlexaFluor546- and AlexaFluor647-transferrin conjugates were obtained from Life Technologies (Grand Island, NY). The Pierce BCA Protein Assay was purchased from Thermo Scientific (Rockford, IL) and used according to manufacturer's instructions. All other materials were obtained as noted in the text. *N*,*N*′-Bis(1-dec-9-enylundec-10-enyl)perylene-3,4,9,10-tetracarboxylbisimide (PERC11) was synthesized as described previously.[57] In brief, perylene-3,4,9,10-tetracarboxyldianhydride was reacted with 1-dec-9-enylundec-10-enylamine (synthesized according to Feiler *et al.*[57]) in the presence of zinc acetate dihydrate and imidazole at 180 °C. The final product was purified by column chromatography on silica gel. The synthesis of the polymerizable surfactant AC10COONa and the liquid crystal nematic cross-linking agent DACTP11 is described elsewhere.[10]

Synthesis of LCNPs. Nanoparticle samples were prepared using a two-phase miniemulsion procedure described previously.[10,11] Briefly, liquid crystalline diacrylate cross-linking agent (DACTP11), perylene dye derivative (PERC11) and a thermal initiator were dissolved in chloroform and added to an aqueous solution of carboxyl-terminated surfactant (AC10COONa). The structures of the LCNP components and a schematic of the miniemulsion procedure are shown in Figure 1. The liquid crystal cross-linker orders and stabilizes the perylene dye molecules into stacked assemblies *via* $\pi-\pi$ molecular orbital interactions. Stirring and sonication of the mixture produced a miniemulsion consisting of small droplets of the organic material surrounded by polymerizable surfactant in water. The mixture was then heated to 64 °C to initiate the polymerization of both the cross-linking agent and surfactant as the organic solvent slowly evaporated to leave a NP suspension stabilized by surfactant. In contrast to other conventional surfactants that are physically adsorbed onto the NP surface and can induce loss of colloidal stability, the polymerizable surfactant used herein covalently binds to the liquid crystal cross-linking agent. Following synthesis, the NP suspension was centrifuged (~8000*g* for 20 min) to reduce the average particle size and sample polydispersity and any aggregated NPs appearing in the pellet were discarded. The LCNPs remaining in the supernatant were then further characterized for their PERC11 perylene dye and DACTP11 liquid crystal content. The materials contained 0.5 and 4.1 mol % of the PERC11 to DACTP11 for the PER103 (green-emitting) and PER104 (red-emitting) LCNPs, respectively.

Characterization of LCNPs. Following their synthesis, the concentration, size and spectral properties of the LCNPs were determined. NP size and concentration were quantified using a NanoSight LM10 imaging system (NanoSight, Ltd., U.K.). The LCNP suspension was serially diluted to visualize the Brownian motion of individual particles within the Rayleigh scattering

regime to assign the average particle size and concentration. For each sample, triplicate experimental runs were performed and averaged. The size of the LCNPs was confirmed by scanning electron microscopy (SEM) using a Leo Supra 55 electron microscope (Carl Zeiss, Inc., Thornwood, NY). Absorbance measurements of diluted LCNP samples were collected on a Cary 5000 UV−vis−NIR spectrophotometer (Agilent Technologies, Santa Clara, CA). The fluorescent emission of LCNP suspensions were collected on a Cary Eclipse Fluorescence Spectrophotometer (Agilent Technologies) using 488 nm excitation. The quantum yield (ϕ), of the LCNPs has been reported previously[10] and was calculated using the comparative method described by Williams *et al.*[58]

Conjugation of LCNPs to Transferrin. PER104 LCNPs were covalently conjugated to human transferrin (Tf) using carbodiimide chemistry. Stock solutions of sulfo-*N*-hydroxysuccinimide (sulfo-NHS, ~55 mM) and 1-ethyl-3-(3-(dimethylamino)propyl) carbodiimide hydrochloride (EDC, ~100 mM) were prepared in HEPES buffer (pH 7.0). An aliquot (10 μL) of EDC solution and 10 μL of sulfo-NHS solution were mixed with 200 μL of a LCNP stock solution (~100 nM) and 270 μL HEPES pH 7.0 and stirred for 15 min. To this solution was added ~5 mg of transferrin protein. After stirring for 2 h, the reaction was briefly centrifuged and the supernatant was subjected to size exclusion chromatography using a PD-10 column equilibrated with PBS. The collected colored band was passed through a 0.2 μM syringe filter and analyzed by 1.5% agarose gel electrophoresis. The concentration of transferrin in the PER104 LCNP conjugates was determined by the bicinchoninic acid (BCA) protein assay using human transferrin as a standard. The average number of transferrin proteins per LCNP was determined by comparison of the protein and LCNP concentrations and corresponded to ~12−15 transferrin molecules per LCNP.

Cell Culture. HEK 293T/17 (ATCC, Manassas, VA) were cultured at 37 °C in a humidified atmosphere containing 95% air/5% CO_2. Cells were cultured in complete growth medium defined as follows: Dulbecco's Modified Eagle's Medium (DMEM, purchased from ATCC) supplemented with 10% (v/v) heat-inactivated fetal bovine serum (ATCC) and 1% antibiotic/antimycotic (Sigma). Cells were cultured in T25 flasks and a subculture was performed every 3−4 days. Cellular NP delivery experiments were performed using cells between passages 3 and 13.

Cellular Delivery of LCNPs. All LCNP delivery experiments were performed on HEK 293T/17 cells that were seeded to the wells (~$1-2 \times 10^4$ cells/well) of LabTek 8-well chambered #1 borosilicate coverglass (Nalge Nunc, Rochester, NY) that were coated with fibronectin (5−10 μg/mL). Stock solutions of LCNP-Tf conjugates were diluted in DMEM-HEPES and incubated on cell monolayers at 37 °C for 1−2 h. The cells were washed with Dulbecco's phosphate buffered saline (D-PBS, pH 7.4) followed by fixation with paraformaldehyde (3.7% in D-PBS) for 10 min. Cell nuclei were stained with DAPI (2 μg/mL in D-PBS) for 10 min at 25 °C. LCNP uptake efficiency (percent signal-positive cells) was determined by analyzing images of at least 50−60 cells collected from random fields. Staggered deliveries for the differential two-color labeling of the recycling endocytic pathway were performed using a sequential two-day delivery regime in which an initial cross section of recycling endosomes was labeled with the first color of LCNP for 30 min to 1 h as described above. The media containing the conjugates was then removed and replaced with complete growth medium and the cells cultured for ~18 h. Following this, a second cross section of recycling endosomes was labeled with the second color of LCNP by incubation of the LCNP-Tf conjugates with cells for 30 min. Cells were then washed, fixed and processed as described above. This two-color labeling technique was performed in two iterations: PER103-Tf (green, day1)/PER104-Tf (red, day 2) and vice versa.

Cellular Imaging of LCNP-Tf Conjugates. Cellular imaging was performed using differential interference contrast (DIC) and epifluorescence microscopy on an Olympus IX-70 inverted microscope equipped with a 60× oil immersion lens. Samples were excited using a Xe lamp and images were collected using filter sets (in parentheses) as follows: nuclei (DAPI), PER103-Tf (fluorescein); PER104-Tf (Texas Red); AlexaFluor 546-Tf (Texas Red); AlexaFluor 647-Tf (Cy5). Details of the filter cube configuration used herein are given in Table S1 (SI). Merged images were generated using DP Manager software (Olympus, ver. 2.2.1.195) and were prepared for publication using Photoshop CS2 (ver. 9.0). The degree of colocalization in the two-color LCNP-Tf experiments was quantified using the JACoP plugin (ver 2.0) within ImageJ (ver. 1.47).[59] This utility determines both the Pearson's correlation coefficient (the statistical measure of the strength of the linear relationship between the fluorescence intensities from the two images) and the percent colocalization of pixels between the two images. For each two-color delivery, five pairs of images (corresponding to a total of 49−81 cells) were analyzed and the Pearson's coefficient and average percent colocalization were determined.

Photostability of LCNP-Tf Conjugates. The intracellular photostability of the LCNP-Tf conjugates was determined by time-resolved imaging of LCNP-Tf-loaded cells while under constant excitation over a 60 s time period. Fluorescence images of HEK 293T/17 cells were acquired every 10 s (~100 ms exposure time) while the sample was under constant excitation. Fluorescence intensities of selected regions of interest (ROI) were quantified using ImageJ. A minimum of 10 ROIs within each image were analyzed and results for each time point were reported as the normalized mean fluorescence intensity relative to control fluorescence intensity at t_0 (initial shutter opening)).

Loading of LCNPs with Dox. LCNPs and LCNP-Tf conjugates were loaded with doxorubicin (Dox) by incubating the LCNPs with a molar excess of Dox. PER104 and PER104-Tf LCNPs (~100 nM final concentration) were incubated with 50 μM Dox in D-PBS for 16 h at 25 °C in the dark with gentle agitation. Unincorporated Dox was removed by size exclusion chromatography using a PD-10 column equilibrated with D-PBS. Differential absorbance spectroscopy on the starting PER104-Tf LCNPs and the Dox-loaded-PER104-Tf LCNPs was used to quantify the concentration of Dox associated with the LCNP-Tf conjugates. Analysis of triplicate preparations revealed the number of Dox molecules associated with the PER104-Tf LCNPs to be 50 ± 9 Dox molecules per LCNP. The Dox remained associated with the NPs for up to one month when stored at 4 °C (data not shown).

LCNP-Tf-Mediated Cellular Delivery of Doxorubicin. The kinetics of LCNP-Tf-mediated Dox delivery were determined by conducting time-resolved cellular delivery, imaging and fluorescence quantification experiments. PER104, PER104-Tf, PER104-Tf-Dox or free Dox were incubated in DMEM-HEPES on HEK 293T/17 cell monolayers for an initial 1 h period. The LCNP concentration used in these experiments was 50 nM. Following this, the media containing the materials was removed, cell monolayers were washed, fresh complete growth medium added, and the cells subsequently cultured for 48 h. At various time points throughout the culture period, the cell cultures were washed, fixed and imaged using fluorescence microscopy to determine the intracellular distribution of the LCNP-Tf conjugates and Dox. The time-resolved accumulation of Dox in cell nuclei and nuclear condensation was determined by the fluorescence imaging of cells that were incubated with free Dox for 1 h then cultured for various time points. Fluorescence intensities and nuclear size of Dox-loaded cells were determined using ImageJ to generate time-resolved standard curves of nuclear Dox concentration and nuclear condensation. At least 10 ROIs each from a minimum of 30 cells were analyzed in replicate experiments after the background fluorescence corresponding to unlabeled cells was subtracted from all images.

Cellular Proliferation Assays. The cytotoxicity of the LCNP conjugates was determined using the CellTiter 96 Aqueous One Solution MTS Cell Proliferation Assay (Promega, Madison WI). This assay measures the proliferation activity of cells that have been incubated with a dose range of LCNP, LCNP-Tf or LCNP-Tf-Dox constructs and is based upon the conversion of a tetrazolium substrate to a soluble formazan product by viable cells following a suitable proliferation period. HEK 293T/17 cells were seeded to the wells of 96-well tissue culture microtiter plates (~5×10^3 cells/well). To each well was added DMEM-HEPES containing increasing concentrations of LCNP-Tf conjugate and

the materials were incubated on the cells for 2 h to emulate the conditions used in NP delivery experiments. After incubation, the materials were replaced with complete growth medium and the cells were cultured for 72 h. After this proliferation period, 20 μL of the tetrazolium substrate was added to each well, and color formation proceeded at 37 °C for 1−2 h. The absorbance of the formazan product was read at 570 nm (absorption minima for the LCNPs used in this study) and 650 nm (for subtraction of nonspecific background absorbance) using a Tecan dual monochromator multifunctional microtiter plate reader (Tecan, U.S.). Absorbance values with the background subtracted were plotted as a function of material concentration and reported as percent of control cell proliferation (degree of proliferation of cells in cell culture media only).

Conflict of Interest: The authors declare no competing financial interest.

Acknowledgment. The authors acknowledge the NRL NSI and Base Funding Program (Work Unit MA041-06-41-4943), DARPA and DTRA JSTO MIPR # B112582M. W. R. Algar is grateful to the Natural Sciences and Engineering Research Council of Canada (NSERC) for a postdoctoral fellowship.

Supporting Information Available: Additional experimental detail and results. This material is available free of charge *via* the Internet at http://pubs.acs.org.

REFERENCES AND NOTES

1. Delehanty, J. B.; Breger, J. C.; Boeneman, G. K.; Stewart, M. H.; Medintz, I. L. Controlling the Actuation of Therapeutic Nanomaterials: Enabling Nanoparticle-Mediated Drug Delivery. *Ther. Delivery* **2013**, *11*, 1411–1429.
2. Sailor, M. J.; Park, J. H. Hybrid Nanoparticles for Detection and Treatment of Cancer. *Adv. Mater.* **2012**, *24*, 3779–3802.
3. Rivera-Gil, P.; Clift, M. D.; Rutishauser, B.; Parak, W. Methods for Understanding the Interaction Between Nanoparticles and Cells. In *Nanotoxicity*; Reineke, J., Ed.; Humana Press: New York, 2012; Vol. 926, pp 33−56.
4. Verma, A.; Stellacci, F. Effect of Surface Properties on Nanoparticle-Cell Interactions. *Small* **2010**, *6*, 12–21.
5. Probst, C. E.; Zrazhevskiy, P.; Bagalkot, V.; Gao, X. Quantum Dots as a Platform for Nanoparticle Drug Delivery Vehicle Design. *Adv. Drug Delivery Rev.* **2013**, *65*, 703–718.
6. Zhou, C.; Yang, S.; Liu, J.; Yu, M.; Zheng, J. Luminescent Gold Nanoparticles: A New Class of Nanoprobes for Biomedical Imaging. *Exp. Biol. Med.* **2013**, *238*, 1199–1209.
7. Oh, E.; Fatemi, F. K.; Currie, M.; Delehanty, J. B.; Pons, T.; Fragola, A.; Lévêque-Fort, S.; Goswami, R.; Susumu, K.; Huston, A. L.; Medintz, I. L. PEGylated Luminescent Gold Nanoclusters: Synthesis, Characterization, Bioconjugation and Application to One- and Two-Photon Cellular Imaging. *Part. Part. Syst. Charact.* **2013**, *30*, 453–466.
8. Zhang, S.; Li, J.; Lykotrafitis, G.; Bao, G.; Suresh, S. Size-Dependent Endocytosis of Nanoparticles. *Adv. Mater.* **2009**, *21*, 419–424.
9. Canton, I.; Battaglia, G. Endocytosis at the Nanoscale. *Chem. Soc. Rev.* **2012**, *41*, 2718–2739.
10. Spillmann, C. M.; Naciri, J.; Wahl, K. J.; Garner, Y. H.; Chen, M.-S.; Ratna, B. R. Role of Surfactant in the Stability of Liquid Crystal-Based Nanocolloids. *Langmuir* **2009**, *25*, 2419–2426.
11. Spillmann, C. M.; Naciri, J.; Anderson, G. P.; Chen, M. S.; Ratna, B. R. Spectral Tuning of Organic Nanocolloids by Controlled Molecular Interactions. *ACS Nano* **2009**, *3*, 3214–3220.
12. Xia, X.-X.; Wang, M.; Lin, Y.; Xu, Q.; Kaplan, D. L. Hydrophobic Drug-Triggered Self-Assembly of Nanoparticles from Silk-Elastin-Like Protein Polymers for Drug Delivery. *Biomacromolecules* **2014**, *15*, 908–914.
13. Kilar, F.; Simon, I. The Effect of Iron Binding on the Conformation of Transferrin. A Small Angle X-Ray Scattering Study. *Biophys. J.* **1985**, *48*, 799–802.
14. Qian, Z. M.; Li, H.; Sun, H.; Ho, K. Targeted Drug Delivery *via* the Transferrin Receptor-Mediated Endocytosis Pathway. *Pharmacol. Rev.* **2002**, *54*, 561–587.
15. Zheng, J.; Ghazani, A. A.; Song, Q.; Mardyani, S.; Chan, W. C.; Wang, C. Cellular Imaging and Surface Marker Labeling of Hematopoietic Cells Using Quantum Dot Bioconjugates. *Lab. Hematol.* **2006**, *12*, 94–98.
16. Qian, J.; Yong, K. T.; Roy, I.; Ohulchanskyy, T. Y.; Bergey, E. J.; Lee, H. H.; Tramposch, K. M.; He, S.; Maitra, A.; Prasad, P. N. Imaging Pancreatic Cancer Using Surface-Functionalized Quantum Dots. *J. Phys. Chem. B* **2007**, *111*, 6969–6972.
17. Tekle, C.; Deurs, B.; Sandvig, K.; Iversen, T. G. Cellular Trafficking of Quantum Dot-Ligand Bioconjugates and Their Induction of Changes in Normal Routing of Unconjugated Ligands. *Nano Lett.* **2008**, *8*, 1858–1865.
18. Delehanty, J. B.; Mattoussi, H.; Medintz, I. L. Delivering Quantum Dots Into Cells: Strategies, Progress and Remaining Issues. *Anal. Bioanal. Chem.* **2009**, *393*, 1091–1105.
19. Delehanty, J. B.; Bradburne, C. E.; Susumu, K.; Boeneman, K.; Mei, B. C.; Farrell, D.; Blanco-Canosa, J. B.; Dawson, P. E.; Mattoussi, H.; Medintz, I. L. Spatiotemporal Multicolor Labeling of Individual Cells Using Peptide-Functionalized Quantum Dots and Mixed Delivery Techniques. *J. Am. Chem. Soc.* **2011**, *133*, 10482–10489.
20. Jennings, T. L.; Becker-Catania, S. G.; Triulzi, R. C.; Tao, G.; Scott, B.; Sapsford, K. E.; Spindel, S.; Oh, E.; Jain, V.; Delehanty; *et al.* Reactive Semiconductor Nanocrystals for Chemoselective Biolabeling and Multiplexed Analysis. *ACS Nano* **2011**, *5*, 5579–5593.
21. Talati, R.; Vanderpoel, A.; Eladdadi, A.; Anderson, K.; Abe, K.; Barroso, M. Automated Selection of Regions of Interest for Intensity-based FRET Analysis of Transferrin Endocytic Trafficking in Normal *vs.* Cancer cells. *Methods* **2013**, *66*, 139–152.
22. ChemSpider. Doxorubicin. CSID:29400, http://www.chemspider.com/chemical-structure.29400.html.
23. El-Kareh, A. W.; Secomb, T. W. Two-mechanism Peak Concentration Model for Cellular Pharmacodynamics of Doxorubicin. *Neoplasia* **2005**, *7*, 705–713.
24. Bagheri, F.; Safarian, S.; Eslaminejad, M.; Sheibani, N. siRNA-Mediated Knock-Down of DFF45 Amplifies Doxorubicin Therapeutic Effects in Breast Cancer Cells. *Cell. Oncol.* **2013**, *36*, 515–526.
25. Aroui, S.; Brahim, S.; De Waard, M.; Bréard, J.; Kenani, A. Efficient Induction of Apoptosis by Doxorubicin Coupled to Cell-Penetrating Peptides Compared to Unconjugated Doxorubicin in the Human Breast Cancer Cell Line MDA-MB 231. *Cancer Lett.* **2009**, *285*, 28–38.
26. Sardão, V.; Oliveira, P.; Holy, J.; Oliveira, C.; Wallace, K. Doxorubicin-Induced Mitochondrial Dysfunction is Secondary to Nuclear p53 Activation in H9c2 Cardiomyoblasts. *Cancer Chemother. Pharmacol.* **2009**, *64*, 811–827.
27. Poon, I. K.; Jans, D. A. Regulation of Nuclear Transport: Central Role in Development and Transformation? *Traffic* **2005**, *6*, 173–186.
28. Kuznetsov, A. V.; Margreiter, R.; Amberger, A.; Saks, V.; Grimm, M. Changes in Mitochondrial Redox State, Membrane Potential and Calcium Precede Mitochondrial Dysfunction in Doxorubicin-Induced Cell Death. *Biochim. Biophys. Acta, Mol. Cell Res.* **2011**, *1813*, 1144–1152.
29. Shi, J.; Wu, X.; Surma, M.; Vemula, S.; Zhang, L.; Yang, Y.; Kapur, R.; Wei, L. Distinct Roles for ROCK1 and ROCK2 in the Regulation of Cell Detachment. *Cell. Death Dis.* **2013**, *4*, e48310.1038/cddis.2013.10.
30. Barua, S.; Mitragotri, S. Synergistic Targeting of Cell Membrane, Cytoplasm and Nucleus of Cancer Cells Using Rod-Shaped Nanoparticles. *ACS Nano* **2013**, *7*, 9558–9570.
31. Qiu, L.-Y.; Yan, L.; Zhang, L.; Jin, Y.-M.; Zhao, Q.-H. Folate-Modified Poly(2-ethyl-2-oxazoline) as Hydrophilic Corona in Polymeric Micelles for Enhanced Intracellular Doxorubicin Delivery. *Int. J. Pharm.* **2013**, *456*, 315–324.
32. Chen, W.; Zhong, P.; Meng, F.; Cheng, R.; Deng, C.; Feijen, J.; Zhong, Z. Redox and pH-Responsive Degradable Micelles for Dually Activated Intracellular Anticancer Drug Release. *J. Controlled Release* **2013**, *169*, 171–179.
33. Wang, T.; Ma, Z.; Wang, C.; Su, Z. A Facile Method for Preparation of Dye-Doped Silica-Based Raspberry-Like

Microspheres and Fluorescent Films. *J. Nanosci. Nanotechnol.* **2009**, *9*, 6594–6599.
34. Vogel, R.; Surawski, P. P.; Littleton, B. N.; Miller, C. R.; Lawrie, G. A.; Battersby, B. J.; Trau, M. Fluorescent Organosilica Micro- and Nanoparticles With Controllable Size. *J. Colloid Interface Sci.* **2007**, *310*, 144–150.
35. Ashley, C. E.; Carnes, E. C.; Phillips, G. K.; Padilla, D.; Durfee, P. N.; Brown, P. A.; Hanna, T. N.; Liu, J.; Phillips, B.; Carter, M. B.; *et al.* The Targeted Delivery of Multicomponent Cargos to Cancer Cells by Nanoporous Particle-Supported Lipid Bilayers. *Nat. Mater.* **2011**, *10*, 389–397.
36. Hu, X.; Hao, X.; Wu, Y.; Zhang, J.; Zhang, X.; Wang, P. C.; Zou, G.; Liang, X.-J. Multifunctional Hybrid Silica Nanoparticles for Controlled DoxorubicinL and Release With Thermal and pH Dual Response. *J. Mater. Chem. B* **2013**, *1*, 1109–1118.
37. Verma, S.; Dent, S.; Chow, B. J. W.; Rayson, D.; Safra, T. Metastatic Breast Cancer: The Role of Pegylated Liposomal Doxorubicin After Conventional Anthracyclines. *Cancer Treat. Rev.* **2008**, *34*, 391–406.
38. Obata, Y.; Tajima, S.; Takeoka, S. Evaluation of pH-Responsive Liposomes Containing Amino Acid-Based Zwitterionic Lipids for Improving Intracellular Drug Delivery *In Vitro* and *In Vivo*. *J. Controlled Release* **2010**, *142*, 267–276.
39. Chakravarthy, K. V.; Davidson, B. A.; Helinski, J. D.; Ding, H.; Law, W. C.; Yong, K. T.; Prasad, P. N.; Knight, P. R. Doxorubicin-Conjugated Quantum Dots to Target Alveolar Macrophages and Inflammation. *Nanomedicine* **2011**, *7*, 88–96.
40. Kong, Y.; Chen, J.; Gao, F.; Brydson, R.; Johnson, B.; Heath, G.; Zhang, Y.; Wu, L.; Zhou, D. Near-Infrared Fluorescent Ribonuclease-A-encapsulated Gold Nanoclusters: Preparation, Characterization, Cancer Targeting and Imaging. *Nanoscale* **2013**, *5*, 1009–1017.
41. Woltman, S. J.; Jay, G. D.; Crawford, G. P. Liquid-Crystal Materials Find a New Order in Biomedical Applications. *Nat. Mater.* **2007**, *6*, 929–938.
42. Lai, S. L.; Huang, S.; Bi, X.; Yang, K.-L. Optical Imaging of Surface-Immobilized Oligonucleotide Probes on DNA Microarrays Using Liquid Crystals. *Langmuir* **2008**, *25*, 311–316.
43. Soon, C. F.; Omar, W. I. W.; Berends, R. F.; Nayan, N.; Basri, H.; Tee, K. S.; Youseffi, M.; Blagden, N.; Denyer, M. C. T. Biophysical Characteristics of Cells Cultured on Cholesteryl Ester Liquid Crystals. *Micron* **2014**, *56*, 73–79.
44. Soon, C. F.; Khaghani, S. A.; Youseffi, M.; Nayan, N.; Saim, H.; Britland, S.; Blagden, N.; Denyer, M. C. T. Interfacial Study of Cell Adhesion to Liquid Crystals Using Widefield Surface Plasmon Resonance Microscopy. *Colloids Surf., B* **2013**, *110*, 156–162.
45. Luck, A. N.; Mason, A. B. Chapter One—Transferrin-Mediated Cellular Iron Delivery. In *Current Topics in Membranes*; José, M. A., Svetlana, L., Eds.; Academic Press: Waltham, MA, 2012; Vol. 69, pp 3−35.
46. Mayle, K. M.; Le, A. M.; Kamei, D. T. The Intracellular Trafficking Pathway of Transferrin. *Biochim. Biophys. Acta, Gen. Subj.* **2012**, *1820*, 264–281.
47. Yin, J.; Lin, A. J.; Buckett, P. D.; Wessling-Resnick, M.; Golan, D. E.; Walsh, C. T. Single-Cell FRET Imaging of Transferrin Receptor Trafficking Dynamics by Sfp-Catalyzed, Site-Specific Protein Labeling. *Chem. Biol.* **2005**, *12*, 999–1006.
48. Luo, H.; Nakatsu, F.; Furuno, A.; Kato, H.; Yamamoto, A.; Ohno, H. Visualization of the Post-Golgi Trafficking of Multiphoton Photoactivated Transferrin Receptors. *Cell Struct. Funct.* **2006**, *31*, 63–75.
49. Zhan, K.; Xie, H.; Gall, J.; Ma, M.; Griesbeck, O.; Salehi, A.; Rao, J. Real-Time Imaging of Rab5 Activity Using a Prequenched Biosensor. *ACS Chem. Biol.* **2011**, *6*, 692–699.
50. Falkowska-Hansen, B.; Falkowski, M.; Metharom, P.; Krunic, D.; Goerdt, S. Clathrin-Coated Vesicles Form a Unique Net-like Structure in Liver Sinusoidal Endothelial Cells by Assembling Along Undisrupted Microtubules. *Exp. Cell. Res.* **2007**, *313*, 1745–1757.
51. Schieber, C.; Bestetti, A.; Lim, J. P.; Ryan, A. D.; Nguyen, T.-L.; Eldridge, R.; White, A. R.; Gleeson, P. A.; Donnelly, P. S.; Williams, S. J.; Mulvaney, P. Conjugation of Transferrin to Azide-Modified CdSe/ZnS Core−Shell Quantum Dots using Cyclooctyne Click Chemistry. *Angew. Chem., Int. Ed.* **2012**, *51*, 10523–10527.
52. Zhang, L.; Tian, L.; Ye, Z.; Song, B.; Yuan, J. Preparation of Visible-Light-Excited Europium Biolabels for Time-Resolved Luminescence Cell imaging Application. *Talanta* **2013**, *108*, 143–149.
53. Lund, F. W.; Wüstner, D. A Comparison of Single Particle Tracking and Temporal Image Correlation Spectroscopy for Quantitative Analysis of Endosome Motility. *J. Microsc.* **2013**, *252*, 169–188.
54. Tacar, O.; Sriamornsak, P.; Dass, C. R. Doxorubicin: An Update on Anticancer Molecular Action, Toxicity and Novel Drug Delivery Systems. *J. Pharm. Pharmacol.* **2013**, *65*, 157–170.
55. Sethuraman, V. A.; Bae, Y. H. TAT Peptide-Based Micelle System for Potential Active Targeting of Anti-Cancer Agents to Acidic Solid Tumors. *J. Controlled Release* **2007**, *118*, 216–224.
56. Sethuraman, V. A.; Lee, M. C.; Bae, Y. H. A Biodegradable pH-Sensitive Micelle System for Targeting Acidic Solid Tumors. *Pharm. Res.* **2008**, *25*, 657–666.
57. Feiler, L.; Langhals, H.; Polborn, K. Synthesis of Perylene-3,4-Dicarboximides—Novel Highly Photostable Fluorescent Dyes. *Liebigs. Annalen.* **2006**, *1995*, 1229–1244.
58. Williams, A. T. R.; Winfield, S. A.; Miller, J. N. Relative Fluorescence Quantum Yields Using a Computer-Controlled Luminescence Spectrometer. *Analyst* **1983**, *108*, 1067–1071.
59. Bolte, S.; Cordelieres, F. P. A Guided Tour into Subcellular Colocalization Analysis in Light Microscopy. *J. Microsc.* **2006**, *224*, 213–232.